

Insights in convective drying of fruit by coupled modeling of fruit drying, deformation, quality evolution and convective exchange with the airflow

Thijs Defraeye ^{a,b}, Andrea Radu ^b

^a *Multiscale Studies in Building Physics, Empa, Überlandstrasse 129, 8600 Dübendorf, Switzerland*

^b *Chair of Building Physics, ETH Zurich, Stefano-Franscini-Platz 5, 8093 Zürich, Switzerland*

Abstract

Coupled modeling of fruit drying, deformation and quality evolution of a half-circular apple fruit slice is combined with modeling of the convective heat and mass exchange with the airflow. The aim was to gain more insight in the fruit drying kinetics, more particular in heterogeneities and couplings in moisture content and shrinkage as well as quality loss within the fruit during drying. Further aims were to investigate the impact of several modeling assumptions and to analyze the effect of the peel on the drying behavior. Large differences in internal moisture distribution and deformation were observed within the fruit slice. They were caused by the complex airflow field around the slice, which induced a spatial variation in convective heat/mass transfer coefficients (CTCs) over the fruit surface. The differences with imposing a single, constant CTC across the fruit surface (non-conjugate approach) indicated the need for including spatially-resolved CTCs (conjugate approach). The impact of including deformation in the model was also quantified. Not accounting for explicit airflow modeling or deformation affected the fruit temperature, and thereby also the fruit quality decay. The presence of a peel affected the drying process and the deformation, resulting in an asymmetrical collapse towards the center of the fruit slice. Coupling the modeled hygrothermal history of the fruit during drying, to fruit quality modeling opens new opportunities for optimizing drying processes. Thereby, the process can be optimized not only in terms of drying time or energy consumption, but also to achieve the best product quality.

Keywords: conjugate; apple fruit; convection; computational fluid dynamics; multiphysics

This document is the accepted manuscript version of the following article:

Defraeye, T., & Radu, A. (2018). Insights in convective drying of fruit by coupled modeling of fruit drying, deformation, quality evolution and convective exchange with the airflow. *Applied Thermal Engineering*, 129, 1026-1038. <http://doi.org/10.1016/j.applthermaleng.2017.10.082>

This manuscript version is made available under the CC-BY-NC-ND 4.0 license <http://creativecommons.org/licenses/by-nc-nd/4.0/>

Introduction

Drying is a key technology to preserve fresh fruits [1]. By drying, off-season availability of these food products and their nutritional content is ensured and food waste is reduced [2,3]. The dried products can also be used further along the value chain (e.g. in breakfast cereals). Dried fruits or derived products, such as fruit leathers, are currently strongly promoted as natural, healthy snacks.

Fruits are however very complex materials and multiple coupled physical and biochemical processes occur during drying [1,4], amongst others: (1) drying, so the removal of moisture; (2) a temperature change due to latent heat of evaporation or when drying at high temperatures; (3) deformation (shrinkage) of the cellular structure of the tissue due to moisture loss, which can also lead to case hardening or cracking; (4) quality loss of active, often heat-sensitive, compounds, including vitamins [5]. In addition, the exchange of heat and mass with the surrounding airflow plays an important role in the drying kinetics, particularly for convective drying processes [4]. The drying process becomes even more complex when the fruits are composite materials [6]. This is the case when a peel is left on a part of the fruit slice, or when another moisture barrier is present. The latter is for example an edible coating or film, which aim to increase shelf life by controlling moisture loss [7,8], or a dehydrating film, which is used to pack fresh-cut fruit prior to drying to preserve quality better during low-temperature drying [9].

Thereby, several complex phenomena are observed during drying of fresh-cut fruit. As a recent example, Defraeye et al. [10] investigated the anisotropic shrinkage of a fruit slice, with the presence of the peel, versus a rather isotropic behavior when the peel was removed. By using quantitative neutron imaging, they could link the deformation to the internal moisture distribution in the fruit (Figure 1). The anisotropic shrinkage for the sample with the peel was assumed to be caused by spatially heterogeneous drying inside the fruit sample, since the peel formed a local barrier to moisture transport. This led to a locally higher moisture content just below the peel, which in turn limited shrinkage there, as both phenomena are coupled. Another reason for the anisotropic shrinkage could also be the mechanical stiffness of the peel. To what extent each effect was contributing remained however an unresolved question.

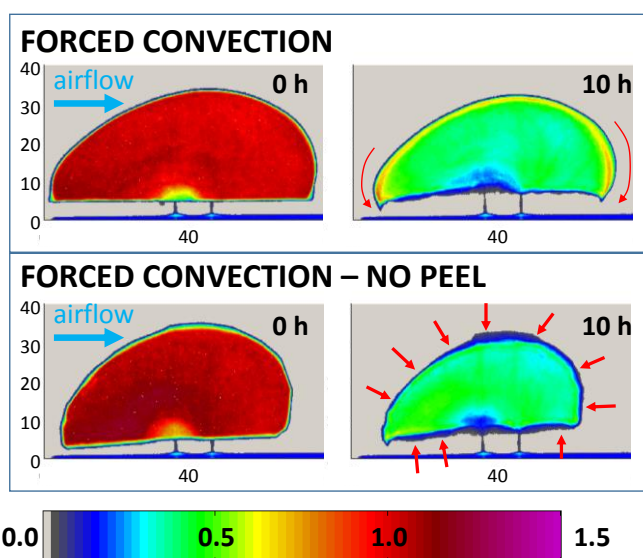


Figure 1. Internal distributions of scaled water content for apple fruit slices with and without peel from neutron radiographs at the start and end of the drying process (adapted from [10]). The same scaling factor is used for all

images. The red arrows illustrate the deformation trend at the end of the drying process. Dimensions are in millimeters.

Non-destructive imaging, for example with neutrons, is found to be very valuable to look at what happens inside the fruit [11–14]. Neutron imaging provides unique quantitative insights on how the internal water distribution evolves during drying (Figure 1). For a better understanding and control of drying processes however, a simultaneous analysis of multiple physical processes and the fruit quality evolution is also essential. Therefore, as an alternative to such experiments, continuum modeling has been applied to analyze the ensemble of coupled processes occurring during drying [4]. From such simulations, high-resolution data is available in time and space on multiple product and process parameters. Such increased insights help defining strategies to provide better product quality, to reduce the residence time in the dryer and thereby also the process energy. Many multiphysics modeling efforts have been made recently on drying of fruits and vegetables [15–19]. However, combining modeling of drying, deformation and quality evolution in the fruit tissue as well as explicit modeling of the convective exchange with the airflow has not been applied to our best knowledge. A detailed knowledge of fruit drying kinetics is however essential to further optimize industrial drying processes [4,20,21].

This study combines the aforementioned processes to investigate low-temperature convective drying of a half-circular apple fruit slice in terms of drying kinetics, deformation and fruit quality loss. Apple fruit is evaluated as it is often used to study fruit drying [22–24] and has a significant economic relevance. Using 3D modeling, we are able to identify and explore heterogeneities and couplings in moisture content and shrinkage as well as quality loss within the fruit during drying. We are also able to identify the effect of the peel on drying and deformation behavior. Furthermore, the impact of different modeling couplings on the drying kinetics is quantified, including the coupling between drying and airflow and the coupling between moisture transport and fruit deformation.

Materials and methods

2.1 Continuum model for drying of fruit tissue

The continuum model consists of several submodels, which are coupled. The following models are solved inside the fruit tissue: a hygrothermal model to simulate fruit drying, a mechanical model to calculate the associated deformation, a fruit quality model to quantify quality evolution. In addition, airflow modeling around the fruit is performed to quantify the convective exchange with the environment. These submodels are detailed separately below, after which their coupling is explained.

2.1.1 Hygrothermal modeling

This model was developed previously [17], where it is described in detail. The following conservation equations for moisture and energy are solved to the dependent variables water potential ψ [Pa] and temperature T [K]:

$$\frac{\partial w_m}{\partial \psi} \frac{\partial \psi}{\partial t} + \nabla \cdot (-K_m \nabla \psi) = 0 \quad (1)$$

$$h_l \frac{\partial w_m}{\partial \psi} \frac{\partial \psi}{\partial t} + (c_{p,s} w_s + c_{p,l} w_m) \frac{\partial T}{\partial t} + \nabla \cdot (-h_l K_m \nabla \psi) + \nabla \cdot (-\lambda_{PM} \nabla T) = 0 \quad (2)$$

where w_s and w_m are the dry-matter density (solid) and moisture content of the tissue [kg m^{-3}], respectively. K_m is the moisture permeability of the tissue [s], h_l is the enthalpy of liquid water [J kg^{-1}], λ_{PM} is the thermal conductivity of the tissue (porous medium) [$\text{W m}^{-1} \text{K}^{-1}$], $c_{p,s}$ and $c_{p,l}$ are the specific heat capacities of dry-matter and liquid water [$\text{J kg}^{-1} \text{K}^{-1}$], respectively. These material properties are given in Table 1. Note that K_m equals 8×10^{-16} s and the apple cultivar is *Braeburn*. Moisture transport is not split up in vapor and liquid water transport, leading to only one conservation equation. Evaporation is assumed to occur only at the air-fruit interface.

To determine the moisture capacity $C_m = \frac{\partial w_m}{\partial \psi}$, the sorption isotherm (w_m vs. water activity a_w) is required (see

Table 1), as well as the relation of water activity a_w to water potential ψ . The latter is given by:

$$\psi = \rho_l R_v T \ln(a_w) \quad (3)$$

The enthalpies of liquid water and water vapor, h_l and h_v [J kg^{-1}], are:

$$h_l = c_{p,l} (T - T_{ref,0}) \quad (4)$$

$$h_v = c_{p,v} (T - T_{ref,0}) + L_v \quad (5)$$

where L_v is the heat of vaporization [J kg^{-1}], also called latent heat, which is the energy needed for the phase change from liquid to vapor. $T_{ref,0}$ is a reference temperature, taken equal to 273.15 K (0 °C).

2.1.1.2 Mechanics modeling

Due to the large deformations which the fruit undergoes during drying, linear elasticity should not be applied and the moisture-induced shrinkage of the tissue needs to be modeled by nonlinear elasticity theory. The fruit tissue is considered here as an isotropic hyperelastic material, which has been applied for several studies on fruits or vegetables [15,16,25]. Viscoelasticity is not considered in this model, as deformations during drying are quite slow [16] and no significant differences with non-viscoelastic modeling were found in the past for apple [25]. The material is assumed to be rubbery during the entire drying process. This is a reasonable assumption for apple fruit, due to the low glass transition temperature, even at low water activities [26]. In this study, the water activity and temperature remain sufficiently high for the fruit tissue to remain above the glass transition temperature, based on reported glass transition temperature data.

The momentum balance during drying is solved assuming a stationary state (no time derivative), due to the slow deformations, and does not account for body or external forces:

$$\nabla \cdot (\mathbf{S}^T \mathbf{F}_{el}^T) = 0 \quad (6)$$

where \mathbf{F}_{el} is the elastic deformation gradient tensor, superscript T is the transpose and \mathbf{S}'' is the second Piola–Kirchhoff stress tensor. For hyperelastic materials, the second Piola–Kirchhoff tensor is described as a function of the elastic strain energy density W_s :

$$\mathbf{S}'' = \frac{\partial W_s}{\partial \mathbf{E}_{el}} \quad (7)$$

where \mathbf{E}_{el} is the elastic Green-Lagrange strain tensor, defined as:

$$\mathbf{E}_{el} = \frac{1}{2} (\mathbf{F}_{el}^T \mathbf{F}_{el} - \mathbf{I}) \quad (8)$$

where \mathbf{I} is the identity tensor and \mathbf{F}_{el} the elastic deformation gradient tensor. To solve the momentum balance, a constitutive relation for W_s is still required. In this study, a Neo-Hookean model is used:

$$W_s = \frac{K}{2} (J_{el} - 1)^2 + \frac{G}{2} (I_1 - 3) \quad (9)$$

where I_1 is the first invariant of the elastic right Cauchy-Green tensor, K is the bulk modulus [Pa] and G is the shear modulus [Pa]. The latter two are defined as:

$$K = \frac{E}{3(1-2\nu)}$$

$$G = \frac{E}{2(1+\nu)} \quad (10)$$

where E is the elastic (Young's) modulus [Pa] and ν is the Poisson ratio [-]. Furthermore, J_{el} is the elastic Jacobian, or the elastic volume ratio ($=\det(\mathbf{F}_{el})$), which can be determined from the total volume ratio J ($=\det(\mathbf{F})$) and the inelastic, moisture-induced deformation J_m ($=\det(\mathbf{F}_m)$) as follows:

$$J_{el} = \frac{J}{J_m} \quad (11)$$

As such, the total deformation is split into an elastic part (\mathbf{F}_{el}) and the moisture-induced deformation part (\mathbf{F}_m). To calculate the moisture induced shrinkage, water transport needs to be linked to the (large) deformations, for which following relation is used, based on [25,27]:

$$J_m = \frac{V(t)}{V_0} = 1 + \varepsilon_{m,vol} = 1 + \frac{V(t) - V_0}{V_0} = 1 + \beta_{vol} (X(t) - X_{ini}) = 1 + \beta_{vol} \left(\frac{w_m(t)}{w_s} - \frac{w_{m,ini}}{w_s} \right) \quad (12)$$

where t is the time, $\varepsilon_{m,vol}$ is the volumetric shrinkage strain, β_{vol} is the volumetric shrinkage coefficient, X is the dry-matter moisture content (w_m/w_s , [kg kg⁻¹]) and X_{ini} is the initial dry-matter moisture content ($w_{m,ini}/w_s$, [kg kg⁻¹]). The volumetric shrinkage coefficient can be derived analytically in such a way that the volume change of the fruit ($V(t) - V_0$) equals the amount (volume) of water lost from the fruit ($V_m(t) - V_{m,0}$). Both terms can be rewritten as:

$$V(t) - V_0 = \beta_{vol} \left(\frac{w_m(t)}{w_s} - \frac{w_{m,ini}}{w_s} \right) V_0 = \beta_{vol} \left(\frac{w_m(t) - w_{m,ini}}{w_s} \right) V_0 \quad (13)$$

$$V_m(t) - V_{m,0} = \frac{m_m(t) - m_{m,ini}}{\rho_l} = \frac{(w_m(t) - w_{m,ini})V_0}{\rho_l} \quad (14)$$

where m_m and $m_{m,ini}$ are the mass of water at a certain point in time [kg], and at the start of the drying process. When assuming that the volume change of the fruit equals the amount of water lost from the fruit, we get:

$$\beta_{vol} \left(\frac{w_m(t) - w_{m,ini}}{w_s} \right) V_0 = \frac{(w_m(t) - w_{m,ini})V_0}{\rho_l} \quad (15)$$

$$\beta_{vol} = \frac{w_s}{\rho_l} \quad (16)$$

Thereby, the moisture Jacobian becomes:

$$J_m = 1 + \frac{1}{\rho_l} (w_m(t) - w_{m,ini}) \quad (17)$$

As we have moisture loss, the Jacobian J_m will be smaller than one, which implies shrinkage. Note that the moisture content, used in the equations above, is based on the undeformed geometry. A model verification was performed in the simulations by checking that the deformation (volume change) equaled the volume of water that was evaporated from the fruit by drying.

Table 1. Material properties, boundary conditions and initial conditions for the base case.

Material properties	Symbol	Value
Moisture permeability fruit tissue [28]	K_m	8×10^{-16} [s]
Thermal conductivity fruit tissue [29]	λ_{PM}	0.418 [$\text{W m}^{-1} \text{K}^{-1}$]
Specific heat capacity of dry matter [29]	$c_{p,s}$	1634 [$\text{J kg}^{-1} \text{K}^{-1}$]
Specific heat capacity of liquid water	$c_{p,l}$	4182 [$\text{J kg}^{-1} \text{K}^{-1}$]
Specific heat capacity water vapor	$c_{p,v}$	1880 [$\text{J kg}^{-1} \text{K}^{-1}$]
Dry-matter density	w_s	130 [kg m^{-3}]
Sorption isotherm (as a function of water activity) [28]	$w_m(a_w)$	$w_s \left(\frac{0.15926}{\ln \left(\frac{1.0177}{a_w} \right)} \right)^{\frac{1}{0.97014}}$ [kg m^{-3}]
Density liquid water	ρ_l	1000 [kg m^{-3}]
Latent heat	L_v	2.5×10^6 [J kg^{-1}]
Specific gas constant for water vapor	R_v	461.52 [$\text{J kg}^{-1} \text{K}^{-1}$]
Poisson ratio	ν	0.495

Elastic modulus	E	5×10^5 [Pa]
Boundary and initial conditions	Symbol	Value
Initial tissue temperature	T_{ini}	20 [°C]
Initial tissue dry-matter moisture content	X_{ini}	6 [kg kg _{dm} ⁻¹]
Initial tissue moisture content	$w_{m,ini}$	780 [kg m ⁻³]
Ambient air temperature	T_{ref}	20 [°C]
Ambient relative humidity	RH_{ref}	30 [%]
Convective heat transfer coefficient (average for non-conjugate modeling)	$h_{c,T}$	13.3 [W m ⁻² K ⁻¹]
Convective mass transfer coefficient (average for non-conjugate modeling)	$h_{c,m}$	9.36×10^{-8} [s m ⁻¹]

2.1.3 Fruit quality modeling

The change of a generic (heat-sensitive) quality attribute A (e.g. enzymatic degradation, vitamin loss) during the drying process is estimated. To this end, a kinetic-rate-law model for the loss of this generic quality attribute is built up [30,31], as detailed in [32]:

$$\frac{-dA}{dt} = kA^n \quad (18)$$

where k is the rate constant [s⁻¹], n is the order of the reaction which dictates if the rate is dependent on the value of A , and t is the time [s]. Both zero-order and first-order reaction kinetics are modeled here. Examples of zero-order reactions are browning as a result of the Maillard reaction, lipid oxidation and enzymatic degradation [30,31]. A first-order reaction is for example vitamin loss. Solving this ordinary differential equation results in a linear decrease (for zero-order) or an exponential decrease (for first order) of the quality attribute over time at a constant temperature:

$$A(t) = A_0 - kt \quad (19)$$

$$A(t) = e^{-kt} + C \quad (20)$$

where A_0 is the quality attribute at the start of the drying process ($t = 0$ s) and C is an integration constant. For the zero-order case, the rate constant k equals the slope of the linear curve. When it is assumed that the initial quality attribute A at $t = 0$ s equals 100%, we get $A_0 = 1$ (100%) and $C = 0$.

To include the dependency of quality decay on the temperature, the rate constant k is expressed as a function of temperature, for which typically an Arrhenius relationship is used:

$$k(T) = k_0 e^{\frac{-E_A}{RT}} \quad (21)$$

where k_0 is a constant [s^{-1}], E_A is the activation energy [$J\ mol^{-1}$], R is the ideal gas constant ($8.314\ J\ mol^{-1}\ K^{-1}$), T is the absolute temperature [K]. To calculate $k(T)$, k_0 and E_A need to be known, which are calibrated based on information of the quality decay. The details of the calibration procedure are described in [32]. Following assumptions are made: (1) $A(20\ ^\circ C, 0\ hours) = 100\% = A_0$; (2) $A_{end}(20\ ^\circ C, 10\ hours) = 70\%$, meaning that after the sample is kept 10 hours at $20\ ^\circ C$, 30% of the quality attribute is assumed to be lost; (3) $Q_{10} = 2$, meaning that an increase in temperature of $10\ ^\circ C$ doubles the rate constant k , so halves the time until all quality is lost. This Q_{10} value equals the ratio of the rate constants at temperatures T and $T+10K$ ($=k_{T+10}/k_T$) and is typically about 2-3 for degradation reactions in fruit [30,33]. These assumptions lead to an E_A of $4.95 \times 10^4\ J\ mol^{-1}$ and a k_0 of $2.00 \times 10^9\ \%\ h^{-1}$ (or $5.57 \times 10^5\ \%\ s^{-1}$) for the zero-order reaction and $2.38 \times 10^7\ \%\ h^{-1}$ (or $6.62 \times 10^3\ \%\ s^{-1}$) for the first-order reaction.

2.1.4 Airflow modeling

Momentum and heat transfer in the air are modeled by solving the Navier-Stokes equations for turbulent flow. Vapor transport in the air is not directly modeled but its influence on the drying process is accounted for by the heat and mass transfer analogy, as detailed below. Turbulence is modeled by applying the Reynolds-averaged Navier-Stokes (RANS) approach in combination with the shear stress transport (SST) $k-\omega$ turbulence model. This is a modification of the standard $k-\omega$ model, proposed by [34]. This model uses a two-equation $k-\omega$ model formulation to solve the near-wall region, for which the $k-\omega$ models were originally developed, while a $k-\epsilon$ model formulation, developed for high-Reynolds number flows, is used to solve the turbulent core region of the flow. This model can improve flow predictions with strong non-equilibrium effects and retains the superior near-wall performance of the $k-\omega$ model [35].

This turbulence model applies a low-Reynolds number modeling (LRNM) approach to model transport in the boundary layer. The boundary layer is explicitly resolved, which requires an extremely high grid resolution at high Reynolds numbers, when LRNM is used to solve the boundary layer. This approach is much more accurate than the commonly used wall functions [36,37], especially for wall friction and convective heat transfer, so for conjugate problems.

Buoyancy effects are not taken into account in the simulations as only forced-convective flow is considered. The assumption essentially means that airflow is not driven by differences in air density caused by temperature gradients. As temperature does not influence the flow field, heat can be considered as a passive scalar.

2.1.5 Solution strategy

A specific solution strategy is applied to solve the different submodels, as they are not solved fully coupled. First, a steady airflow calculation is performed to extract the spatial distribution of the convective heat transfer coefficients. Afterwards, a transient drying calculation is performed to solve for heat and moisture transfer during drying, coupled with the associated deformation. Finally, this drying data is used to solve the kinetic quality model to predict the quality evolution at different points in time. The relevant submodels were verified and validated previously by the authors [17,25,36] including for drying kinetics and temperature. Exactly these variables (drying rate and

temperature, where the latter is linked to quality) are of interest in the present study. The coupling procedure was verified as well.

The coupling between the airflow and the fruit implies a semi-conjugate approach to account for the convective exchange of heat and moisture between the fruit and the air at their interface. This implies that the spatial distribution of the convective heat and mass transfer coefficients over the fruit surface is determined a-priori by an airflow calculation. These convective transfer coefficients (CTCs) at the fruit surface are then used afterwards in the drying simulation. Such a semi-conjugate approach is more accurate and specifically targeted for the fruit geometry of interest, in contrast to the non-conjugate approach. For the latter, CTCs are estimated from existing empirical correlations, for which often a single value is used for the entire fruit, although a spatial CTC variation exists [38,39]. Furthermore, such spatially-constant CTCs have often been determined for a different geometry as the one of interest, in this case being a half-circular fruit slice. A fully-conjugate simulation on the other hand, where transport in the fruit and airflow domains are solved simultaneously in a transient way, would significantly increase the calculation time but not necessarily the accuracy, as [40] showed recently for fruit drying. The choice for the semi-conjugate modeling in this study is a compromise between accuracy and computational cost for the 3D problem.

Finally, the fruit quality modeling is performed using the time-temperature profile of the volume-averaged fruit temperature during drying. It is performed after – and not during – the hygrothermal calculation for three reasons, which make it a viable assumption: (1) the temperature gradients within the sample are small; (2) the time scales for heat transfer were much smaller than those of the drying process and the associated the quality loss; (3) the computational time of the transient drying calculation was reduced.

2.1.6 Coupling at the air-fruit interface

To couple the airflow domain to the fruit tissue, following boundary conditions at the air-tissue interface (continuity of fluxes) are specified:

$$\mathbf{n} \cdot (-K_m \nabla \Psi) = g_m = h_{c,m} (p_{v,w} - p_{v,ref}) \quad (22)$$

$$\mathbf{n} \cdot (-h_l K_m \nabla \Psi - \lambda_{PM} \nabla T) = g_T = (h_{c,T} (T_w - T_{ref}) - h_v g_m) \quad (23)$$

where g_m [$\text{kg m}^{-2} \text{s}^{-1}$] and g_T [$\text{J m}^{-2} \text{s}^{-1}$] are the mass and heat fluxes at the interface, \mathbf{n} is the unit vector normal to the interface, $h_{c,m}$ is the convective mass transfer coefficient (CMTTC [s m^{-1}]), $h_{c,T}$ is the convective heat transfer coefficient (CHTC [$\text{W m}^{-2} \text{K}^{-1}$]), $p_{v,w}$ and $p_{v,ref}$ are the vapor pressures at the interface and of the ambient air [Pa], T_w and T_{ref} are the temperatures at the interface and of the ambient air [K], h_v and h_l are the enthalpies of water vapor and liquid water [J kg^{-1}].

The vapor pressures $p_{v,w}$ and $p_{v,ref}$ are determined based on the water activity at the interface ($a_{w,w}$) and the relative humidity of the environment during drying or tempering (RH_{ref}), respectively, together with the corresponding temperatures, via the saturated vapor pressure ($p_{v,sat}$ [Pa]):

$$p_{v,w} = a_{w,w} p_{v,\text{sat}}(T_w) \quad (24)$$

$$p_{v,\text{ref}} = RH_{\text{ref}} p_{v,\text{sat}}(T_{\text{ref}}) \quad (25)$$

$$p_{v,\text{sat}}(T) = e^{65.8094 - \frac{7066.27}{T} - 5.976 \ln T} \quad (26)$$

For heat transfer, the boundary condition states that heat loss from the tissue, due to conduction and liquid water transport, equals the convective (sensible) heat exchange with the environment and the heat removal due to the water vapor loss, including evaporation. For mass transfer, the boundary condition states that the moisture loss from the tissue equals the convective vapor removal from the surface.

2.2 Configuration and computational model

Forced convective drying of a single fresh-cut apple slice, suspended in free-stream turbulent airflow, is modeled. A half-circular slice (diameter $D = 50$ mm, thickness 10 mm) is considered, in contrast to the often rectangular-shaped geometries that have been evaluated so far for apple fruit. A 3D model is constructed, where only half of the slice is modeled due to symmetry. The base case and the variants that are simulated are detailed below (Table 2).

2.2.1 Base case

The computational model and the imposed boundary conditions are specified in Figure 2. The upstream and downstream sections of the computational domain are taken sufficiently long to avoid an influence from inlet and outlet boundary conditions on the airflow in the vicinity of the fruit. Also the lateral boundaries are placed at a significant distance from the fruit.

Air domain

At the domain inlet, a uniform bulk speed of 0.5 m s^{-1} is imposed (U_b), which results in a Reynolds number of about 1600 for the base case, based on U_b and D . A limited turbulence intensity (5%) is imposed at the inlet. The free-stream approach flow is kept at a constant temperature ($T_{\text{ref}} = 20 \text{ °C}$) and relative humidity ($RH_{\text{ref}} = 30\%$). At the outlet of the computational domain, a zero static pressure is imposed. The lateral boundaries are modeled as slip-wall boundaries (symmetry), which assume that the normal velocity component and the normal gradients at the boundary are zero. The interface of the air with the fruit is modeled as a no-slip boundary for momentum transport, but exchange of heat (and moisture) between the two domains is enabled (see section 2.1).

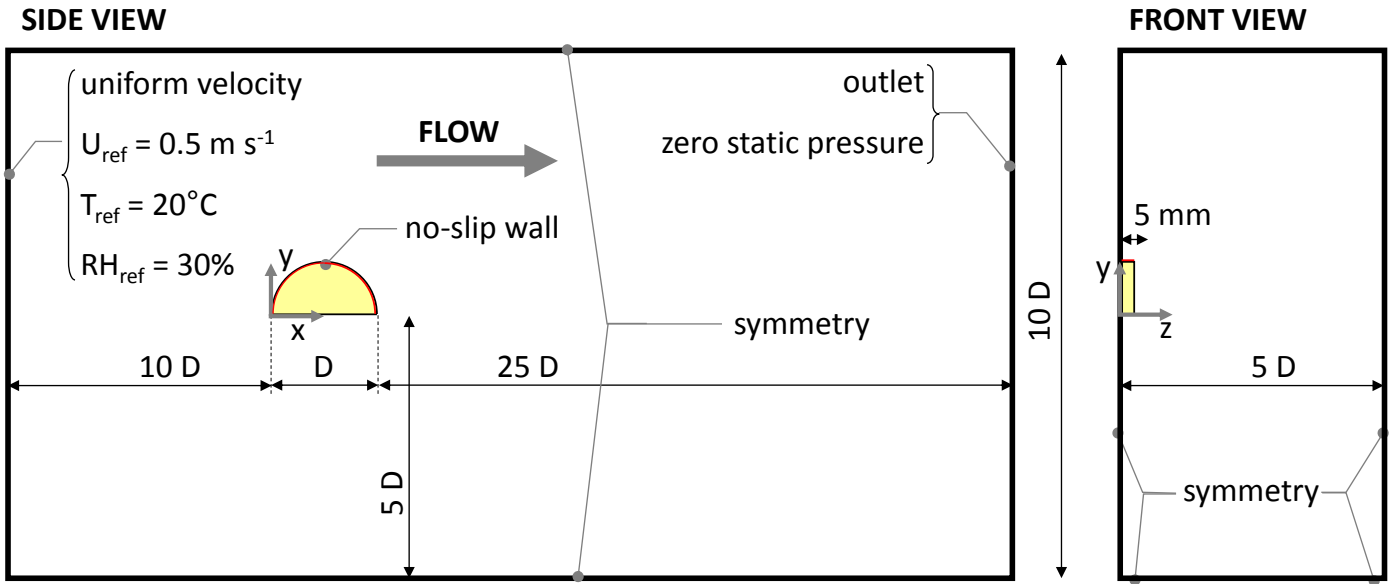


Figure 2. Computational domain (not to scale) and boundary conditions. The red line represent the location of the peel.

Fruit domain

The porous material is apple fruit (cv. *Braeburn*). The relevant material properties are specified in Table 1. The fruit is assumed to be initially (fresh-cut state) at a uniform moisture content $w_{m,ini}$ of 780 kg m^{-3} at a uniform temperature T_{ini} of 20°C . This moisture content leads to a dry-base moisture content X_{ini} of 6 ($= w_{m,ini}/w_s [\text{kg kg}_{dm}^{-1}]$).

To calculate the convective heat and mass exchange with the airflow, CTCs are imposed at the fruit surface. Note that only the CHTC is calculated by the semi-conjugate approach, and the CMTC is estimated from the CHTC using the heat and mass transfer analogy, similar as in [41]. The corresponding CMTC/CHTC ratio (analogy factor) is 7.03×10^{-9} .

The boundary conditions for the mechanical modeling are quite straightforward. All boundaries are taken free, apart from two constraints which needed to be imposed for numerical stability: the center plane of the fruit was treated as a symmetry plane, and one point in the middle of the fruit, in this symmetry plane, needed to be fixed in all directions.

An appropriate grid is built for the air and fruit material domains, based on a grid sensitivity analysis. The hybrid grid (tetrahedral and prismatic finite elements) consists of 632 486 elements for the fruit domain and 1 339 759 elements for the air domain, leading to a total of 1 972 245 elements. A gradual refinement towards the air-porous material interface is used to enhance numerical accuracy and stability, as the largest gradients occur there at the start of the drying process. As mentioned, the grid in the boundary layer on the fruit surface was taken sufficiently fine to enable low-Reynolds number modeling. In the present study, long-wave radiation exchange of the tissue with the environment via the surface was not included.

2.2.2 Variants

Different types of variants are simulated (Table 2). A first variant (NonConj, Table 2) evaluates the non-conjugate approach. Here, spatially-constant CHTC and CMTC values are imposed on all sides of the fruit slice during the entire

drying process. These values are the surface-averaged CTCs from the airflow calculation, which are reported in Table 1. A second variant (NoDeform) evaluates the case without moisture-induced deformation, so just drying. A third variant (NonConj-NoDeform) evaluates the non-conjugate approach without deformation. The fourth variant (WithPeel) evaluates the case with a peel. To this end, the peel is modeled as an impermeable moisture (not thermal) barrier and is covering the entire side of the half-circular slice (Figure 2).

Table 2. Drying conditions for different variants. If no value is specified (indicated by a dash), the same one is taken as the base case.

Variant name	Airflow modeling	Deformation modeling	With/without peel	Remark
Base case	semi-conjugate	yes	Without	
NonConj	non-conjugate	-	-	non-conjugate approach
NoDeform	-	no	-	without moisture-induced deformation
NonConj-NoDeform	non-conjugate	no	-	non-conjugate approach without deformation
WithPeel	-	-	With	with a peel

2.3 Numerical simulations

This model was implemented in COMSOL Multiphysics (version 5.2), which is finite-element based commercial software. For turbulent airflow modeling, the computational fluid dynamics (CFD) module of COMSOL was used, using a segregated solver, relying on the PARDISO solver scheme. To solve the hygrothermal transport in the fruit, the partial differential equation interface (coefficient form) was used, in which the aforementioned conservation equations were implemented. Linear shape functions were used here. To solve mechanical deformation, the structural mechanics module was used with the hyperelastic (Neo-Hookean) material model and linear shape functions. Hygrothermal transport and mechanical deformation were solved using a fully coupled solver, relying on the MUMPS solver scheme. The fruit quality was solved separately, based on the temperature-time history of the fruit.

The tolerances for convergence and other solver settings were determined based on sensitivity analysis. After the steady airflow calculation, the CTCs on the fruit surface were extracted and a drying process of 40 hours was simulated, starting from the specified initial conditions. All simulations applied adaptive time stepping, with a maximal time step of 600 s, as determined from a temporal sensitivity analysis. Convergence was monotonic in all cases.

3. Results and discussion

3.1 Airflow and CTCs

First, the airflow around the fruit slice and the corresponding distribution of the convective heat transfer coefficient (CHTC) on the fruit surface are analyzed for the base case. Note that the convective mass transfer coefficient was directly related to the CHTC via the analogy, so the CHTC distribution is also representative for that of the CMTC.

In Figure 3, the air speed around the fruit slice is shown in different planes. In Figure 4, the corresponding CHTC on the fruit surfaces is shown for the base case for different projections. For some projections, the air speed in the symmetry plane is also included. In Figure 5, the CHTC is shown for various scaling, in order to illustrate more clearly its magnitude and distribution on the surface. Note that the surface-averaged value of the CHTC was $13.3 \text{ W m}^{-2}\text{K}^{-1}$.

At the windward part of the half-circular slice surface, higher CHTCs are found due to the flow impinging onto this surface. At the leeward side, a clear wake zone is present, inducing low CHTCs there. The CHTC distribution on the side surface, on the other hand, is quite uniform. The heterogeneous distribution of CHTCs (so CMTCs) over the fruit slice surface will affect the simulated drying behavior, compared to using a constant value over the entire fruit surface. Such a non-conjugate approach is often applied, instead of the semi-conjugate approach used in the base case, and the differences are discussed in section 3.3.1.

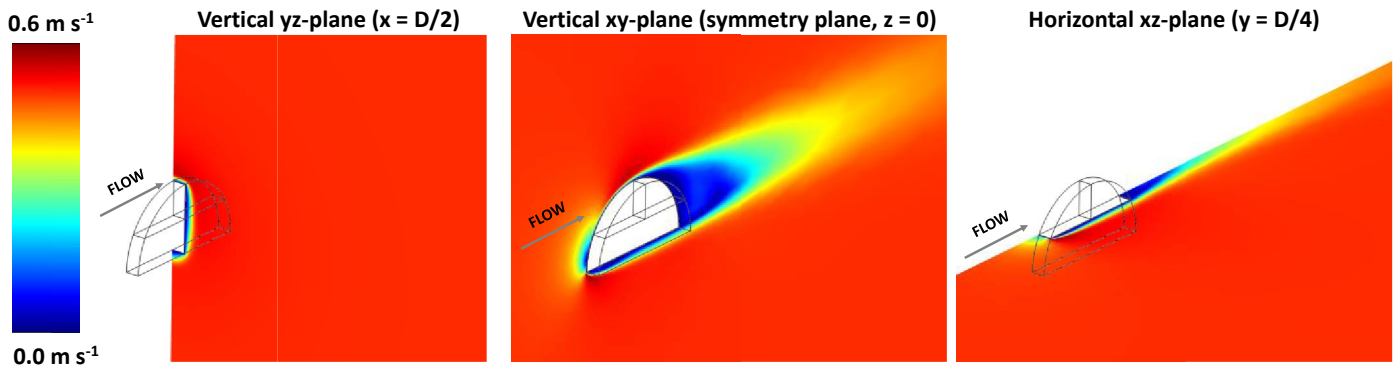


Figure 3. Air speed around the fruit slice in different horizontal and vertical planes for the base case (axis is specified in Figure 2).

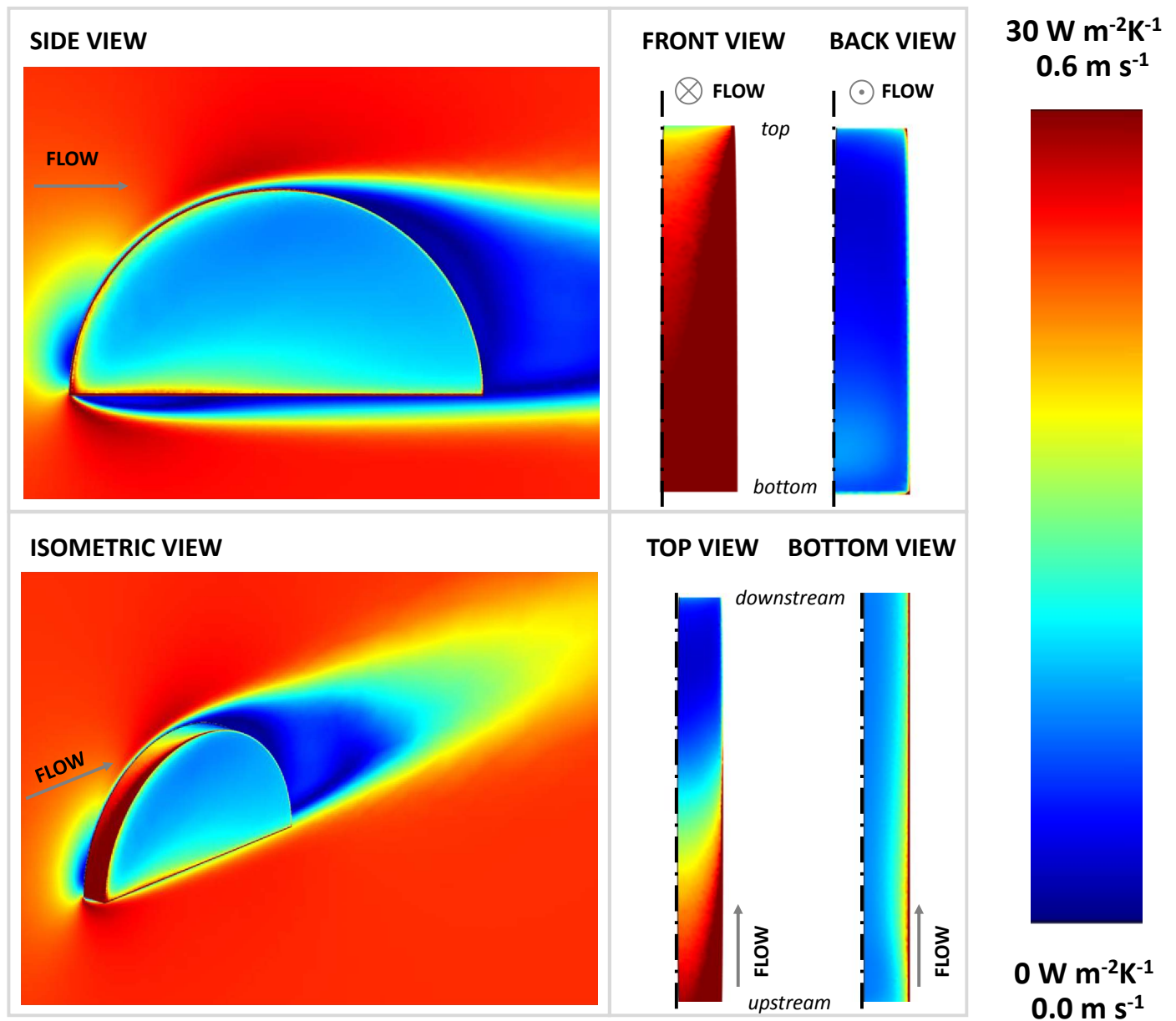


Figure 4. Convective heat transfer coefficient distribution on the fruit slice surface for different views for the base case. In the side and isometric view, the air speed in the symmetry plane ($z = 0$) is also shown. Note that the CHTC range, depicted in the color bar, does not represent the full range and does not include the highest CHTC value.

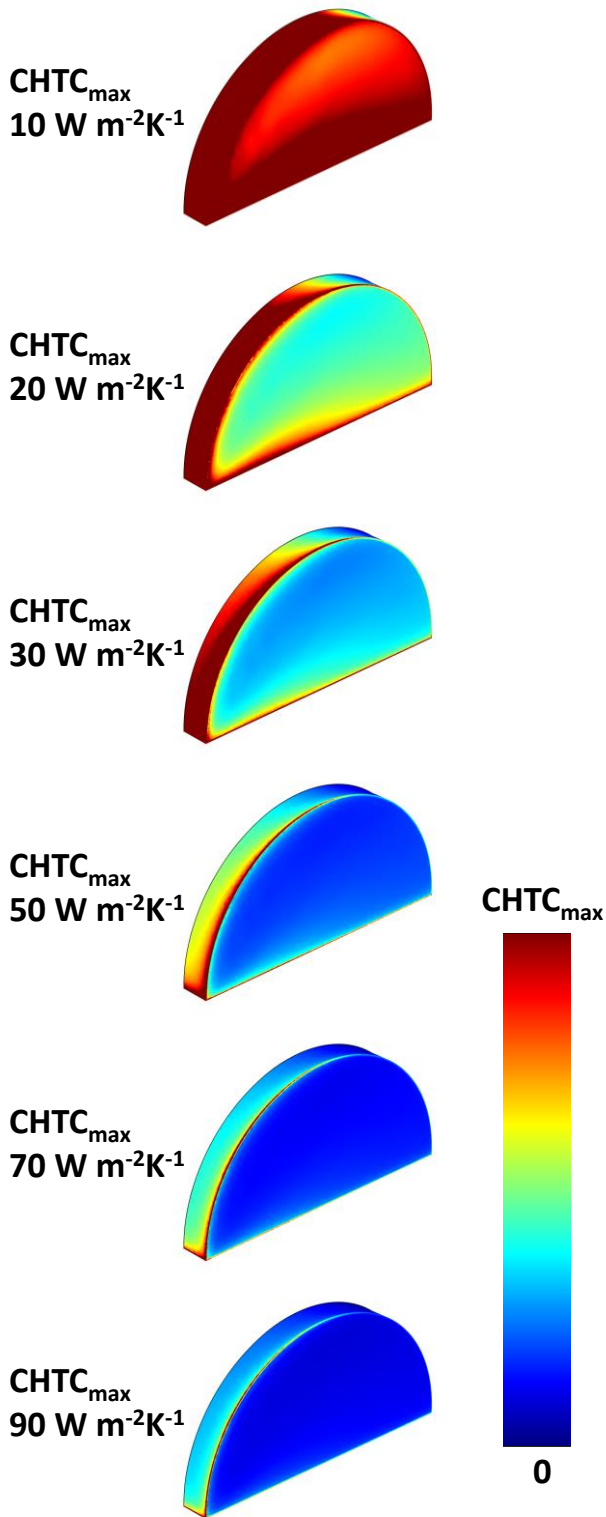


Figure 5. Convective heat transfer coefficient (CHTC) distribution on the fruit slice surface for the base case for different scaling, i.e. values of the maximal CHTC that is depicted. Note that the CHTC range, depicted in the color bar, does not represent the full range and does not include the highest CHTC value.

3.2 General drying characteristics

3.2.1 Overall drying kinetics

First, the overall drying kinetics are analyzed for the base case. In Figure 6, the dry-matter moisture content and surface-averaged mass flux (drying rate) are shown versus time, as well as the temperature and water activity in the

fruit slice. For the latter two, the volume-averaged values and surface-averaged values (at the air-fruit interface) are given, as well as the minimal and maximal values in the fruit slice.

In addition, analytical predictions of the drying rate in the constant drying rate period (CDRP) and the corresponding mass loss are also shown, as well as the wet bulb temperature. The CDRP is found during the first stage of the drying process and is characterized by a high relative humidity (RH) at the surface ($\approx 100\%$), an almost constant drying rate and a constant material temperature, which is close to the wet bulb temperature (T_{wb}). During the CDRP, the convective heat supply to the interface is quasi entirely used for the evaporation of water. The CDRP drying rate can be estimated analytically based on a simplified heat balance, as detailed in [17], for example. This heat balance assumes that no radiative heat flows at the surface are present as well as no (conductive) heat flows from the interior of the porous material. Furthermore, a moist surface (RH $\approx 100\%$) is assumed which is at the wet bulb temperature.

The critical dry-matter moisture content X_{crit} is also shown in Figure 6 [17]. This is the (volume-)averaged dry-matter moisture content in the sample that corresponds, via the sorption isotherm, to an equilibrium water activity below which no spoilage occurs ($a_{w,crit}$). For dried fruit, this $a_{w,crit}$ is about 0.6 [3]. In principle, if the drying process is stopped at X_{crit} and the sample is equilibrated in an environment where the humidity corresponds to $a_{w,crit}$ or lower, the average final water activity in the tissue will be below $a_{w,crit}$. Thereby, the critical moisture content can be used as a criterion to end the drying process, by which a sufficiently dry fruit is obtained to avoid spoilage. For the present study, X_{crit} was $0.29 \text{ kg kg}_{dm}^{-1}$, leading to a critical moisture content $w_{m,crit}$ of 37.8 kg m^{-3} . The time to reach X_{crit} , namely the critical drying time t_{crit} , enables to compare multiple drying processes quantitatively in a more straightforward way than based on drying curves (e.g. Figure 6). The reason is that the drying kinetics are summarized into a single value, instead of a curve.

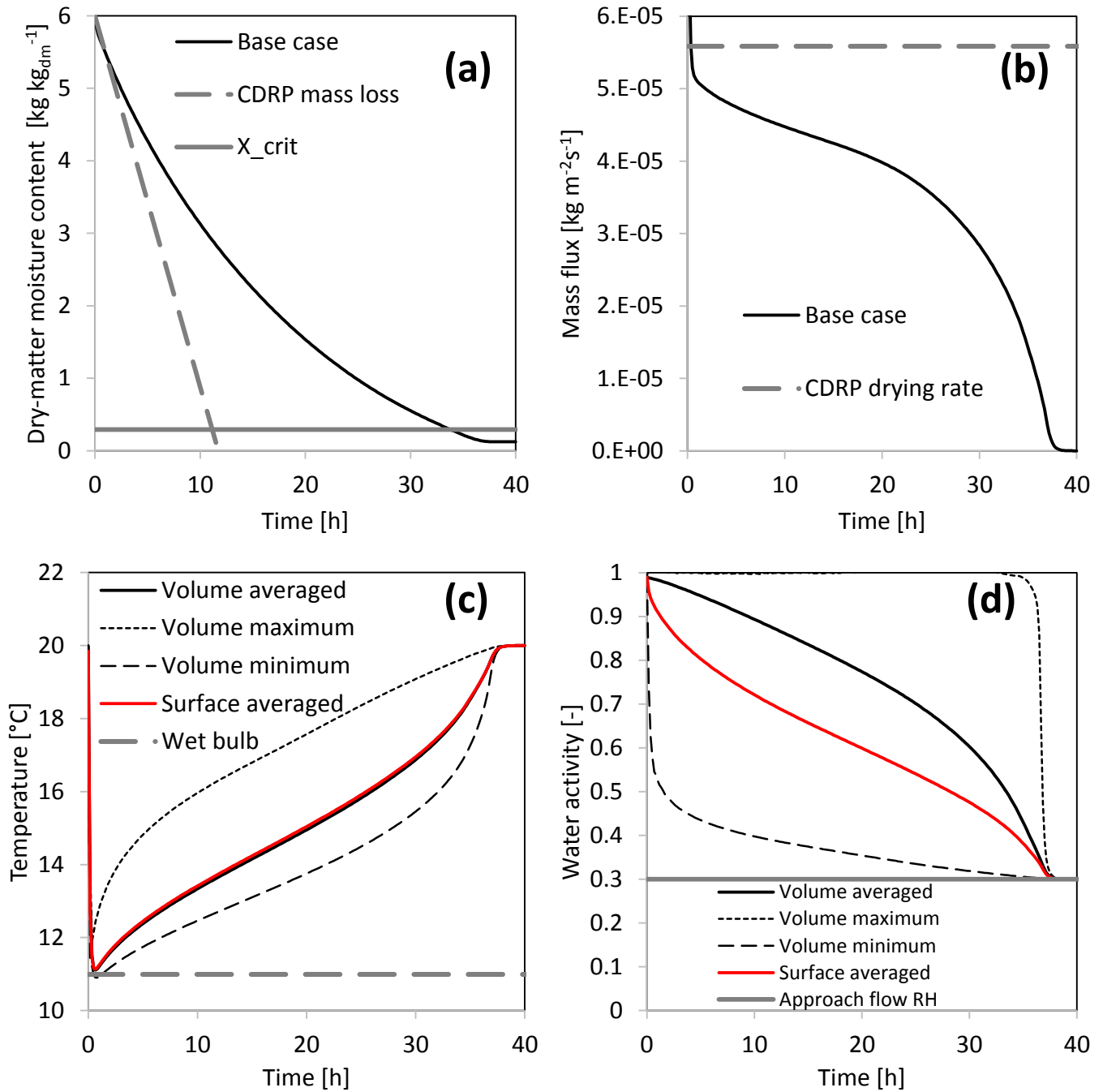


Figure 6. Different drying process parameters for the base case: (a) dry-matter moisture content X , based on the initial volume of the fruit slice, where the critical moisture content X_{crit} is also included; (b) surface-averaged mass flux (drying rate); (c) volume- and surface -averaged temperature (at air-fruit interface) as well as maximal and minimal values in the fruit slice; (d) corresponding water activity. The analytically-determined mass loss and drying rate for CDRP (constant drying rate period) conditions as well as the wet bulb temperature are indicated with the dashed grey lines.

From Figure 6, it is clear that a CDRP is not present, even though the drying conditions (U_b , T_{ref} , RH_{ref}) are rather mild. The occurrence of a CDRP and its length are strongly dependent on the drying conditions and the moisture permeability of the tissue [17]. Most fruits are reported to have a very short CDRP or no CDRP at all, including apples [39,42,43]. Nevertheless, the used analytical indicators for the CDRP help to verify in a very straightforward way if the predicted magnitude of the drying kinetics are realistic.

The impact of moisture removal on the temperature is clearly visible: due to the energy needed to evaporate water from the fruit, its temperature decreases. Due to the slow evaporation process, rather small temperature variations are found within the fruit (results not shown), rendering surface and volume-average temperatures almost equal. However, there are local extreme values, as reflected by the minimal and maximal temperatures, which are caused by the complex flow field around the fruit and the differences in drying between windward and leeward surfaces.

In addition, the change in moisture content is given in Figure 7, where it is defined in two different ways: (1) based on the initial volume $w_m(t) = m_m(t)/V_0$, where m_m is the mass of water inside the fruit [kg] and V_0 is the initial volume of the fruit slice [m^3]; (2) based on the instantaneous volume (V) of the sample $w'_m(t) = m_m(t)/V(t)$. The reason for considering these two definitions is that in experiments, the mass of the sample is often measured gravimetrically to determine the moisture content (so w_m), but, at best, only the initial volume V_0 is determined. Measuring the volume change is often too time consuming. In reality however, the true moisture content w'_m will change in a different way during drying. From Figure 7, both moisture contents differ, as expected, where w'_m decreases slower due to the simultaneous decrease of the volume V , in addition to the amount of water in the fruit m_m . Nevertheless, the critical drying time, i.e. when the moisture content reaches $w_{m,crit}$ and which can be used as a criterion to stop the drying process, is approximately the same for both definitions. Note that, unless specified otherwise, w_m (not w'_m) is used in the present study when moisture content is discussed.

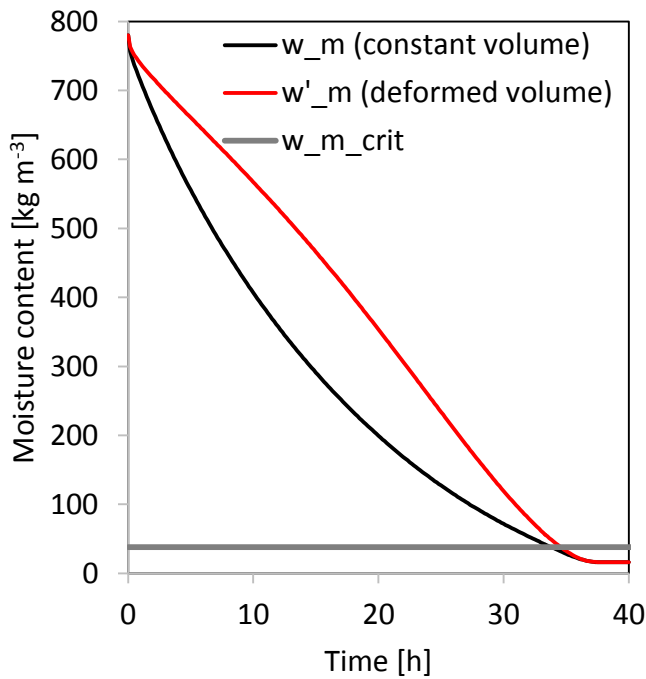


Figure 7. Dry-matter moisture content, based on the initial volume ($w_m = w_m$) of the fruit slice and on the deformed volume ($w'_m = w'_m$), as a function of time for the base case. The critical moisture content $w_{m,crit}$ ($w_{m,crit}$) is also included.

3.2.2 Heterogeneity in drying

Next to the overall drying kinetics, the spatial variation in drying kinetics within the fruit is looked at in more detail. In Figure 8, the distribution of the water activity in the center of the fruit slice is shown (symmetry plane, $z = 0$) at different points in time for the base case. The other variants are also shown for comparison, but are discussed below in section 3.3. The spatial variation in moisture distribution within the fruit is clear, showing highly differential drying

within the fruit. The windward side clearly dries faster than the leeward side, where the zone in the fruit that is adjacent to the recirculation zone at the leeward side remains moist for a long time. The impact of including detailed airflow modeling, by the semi-conjugate approach, for drying predictions is obvious.

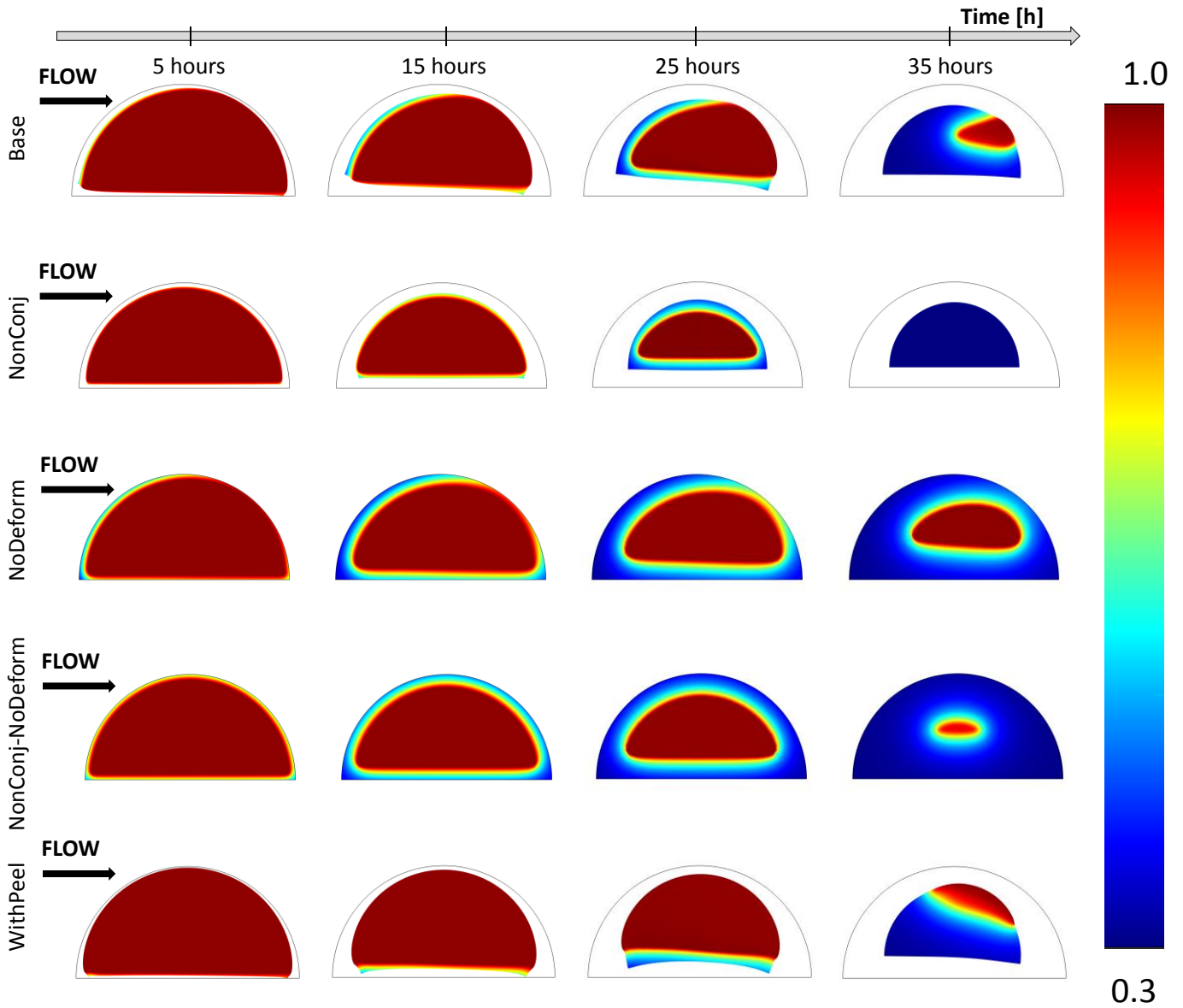


Figure 8. Water activity a_w in the center of the fruit (in the symmetry xy -plane for $z=0$) at different points in time for the base case and the different variants. The abbreviations are detailed in Table 2.

3.2.3 Deformation

As shown in Figure 8, the deformation is clearly not symmetrical for the base case, caused by the spatial differences in drying rates. As more drying occurs near the windward side (left side in Figure 8), the deformation, which is proportional to the amount of water removed, is larger there. Note that deformation was only related to moisture loss and no case hardening or other type of deformation-induced change in the mechanical properties of the material was included in the model. As a result, the final deformed geometry after full drying will not contain this asymmetry seen during the drying process anymore as the majority of the water is removed everywhere.

3.2.4 Fruit quality

The fruit quality evolution is shown in Figure 9 for both zero-order and first-order reaction kinetics for the base case and other variants. The dots in the graphs indicate the critical drying time t_{crit} for each simulation, so when the fruit slice is considered to be sufficiently dry. In addition, the quality loss at a constant temperature of 10 °C and 20 °C is also shown. For the base case, roughly 30% (zero-order) to 35% (first order) of the quality attribute is maintained once the product reaches the critical drying time. Due to the varying fruit temperature, the quality decay clearly deviates from the constant temperature profiles for both zero-order and first-order reaction kinetics.

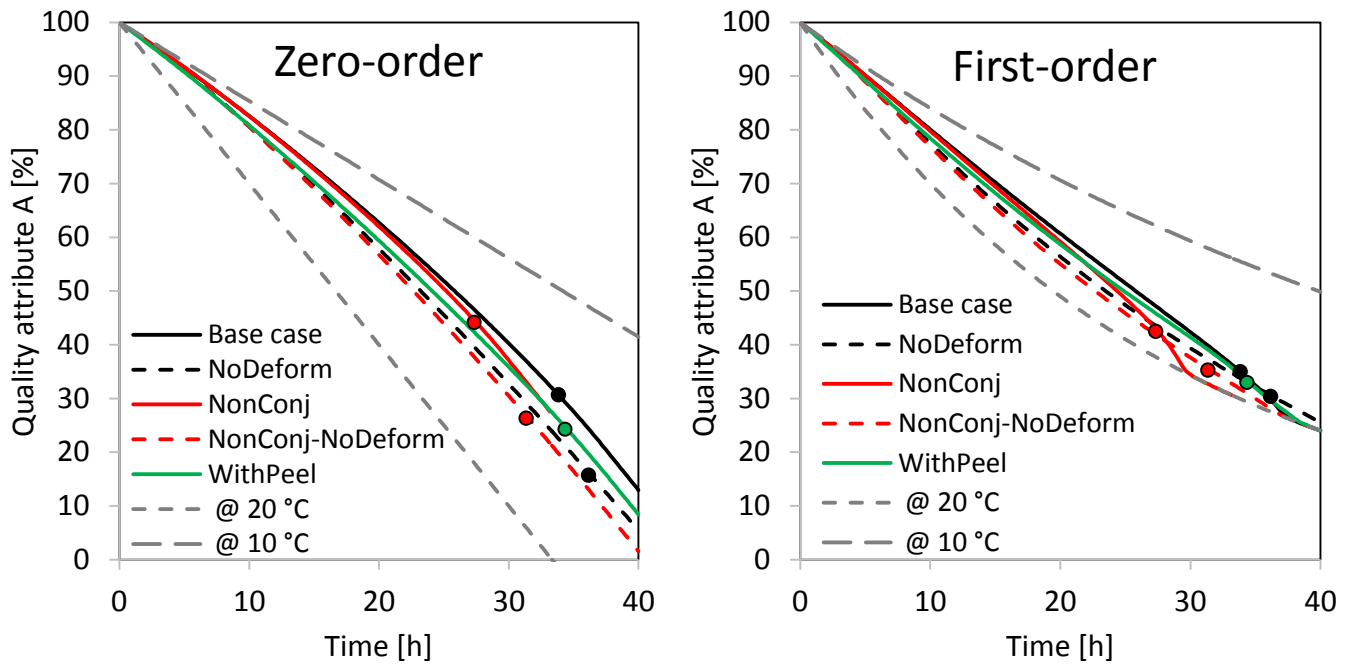


Figure 9. Comparison of drying process simulations of the base case and other variants in terms of the quality attribute A as a function of drying time for zero- and first-order reaction kinetics. The dots indicate the end of the drying process for each variant, namely when the critical dry-matter moisture content is reached. The dashed grey lines indicate the decay at constant temperature ($A(t, 10\text{ °C})$ and $A(t, 20\text{ °C})$). The abbreviations are detailed in Table 2.

3.3 Impact of modeling assumptions

3.3.1 Semi-conjugate approach vs. non-conjugate approach

In Figure 10, the dry-matter moisture content is shown versus time for different variants, as well as the average temperature and water activity on the surface of the fruit slice. In addition, the change in volume (V) over time is also shown, scaled with the initial volume V_0 , which thereby represents the Jacobian J_m (Eq.(17)). Compared to the base case (semi-conjugate approach), the non-conjugate approach (full red line) exhibits a higher drying rate, and, as a result of that, also faster shrinkage.

The differences found in drying kinetics in this study between non-conjugate and semi-conjugate approaches are quite significant. This contrasts the much smaller differences that were observed between a fully-conjugate approach and a non-conjugate approach for 2D drying of a fruit slice [40]. The main reason for this mismatch is attributed to the 2D-3D modeling difference. Although both models had a very non-uniform CTC distribution over their surfaces, the 3D geometry of the fruit slice particularly exhibits large differences in CTCs between the lateral and streamwise surfaces, so between the half-circular part (top and bottom view in Figure 4) and the side surface (side view in Figure 4). The surface averaged CHTC for the entire fruit slice is $13.3 \text{ W m}^{-2} \text{ K}^{-1}$, whereas that for the half circular part equals $16.3 \text{ W m}^{-2} \text{ K}^{-1}$ and that of the side surface equals $11.4 \text{ W m}^{-2} \text{ K}^{-1}$. As such, for the non-conjugate case, a constant (i.e. surface-averaged) CHTC is imposed on the side surface ($13.3 \text{ W m}^{-2} \text{ K}^{-1}$) which is actually higher than the value found for the semi-conjugate approach ($11.4 \text{ W m}^{-2} \text{ K}^{-1}$). This makes that the non-conjugate model will exhibit faster drying on the side surface and slower drying via the half-circular part. Since the distance for moisture to travel from the fruit center to the side surface is shorter, due to the small thickness of the fruit, the overall drying will be faster for the non-conjugate case. The difference between non-conjugate and semi-conjugate (or full-conjugate) modeling will be less obvious for larger slice thicknesses, and was found to be small for 2D modeling [40]. For the 3D model, full conjugate modeling would be computationally very expensive, as the airflow field would need to be resolved every time step as well. Nevertheless, this could improve realism even more as then also the temporal variation of the CTCs is captured as well.

The spatial uniformity in drying within the fruit slice is assessed via Figure 8, where the differences in water activity distributions between non-conjugate and semi-conjugate strategies (base case) are compared. The non-conjugate case dries symmetrically from all sides. Also note that the differences between minimal and maximal temperatures in the fruit slice were much smaller (results not shown) than those for the semi-conjugate case (Figure 6c), and they were even below 1°C . The shrinkage for the non-conjugate case is also symmetrical, as it is directly related to the moisture loss. Finally, a bit more quality loss appears in the non-conjugate case (Figure 9), as the temperature is slightly higher (Figure 10c).

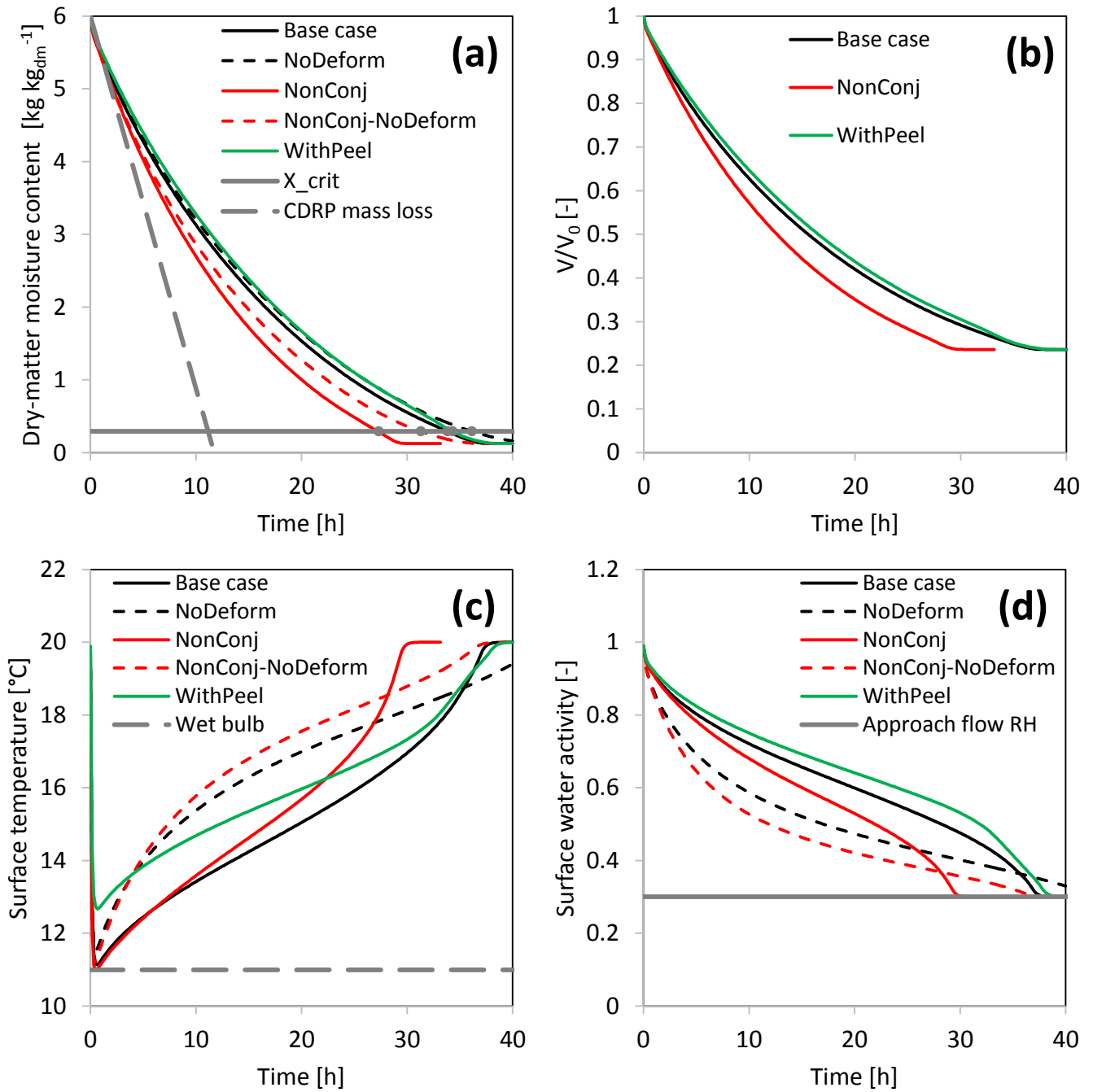


Figure 10. Different drying process parameters for the base case and other variants: (a) dry-matter moisture content, based on the initial volume of the fruit slice, where the critical moisture content X_{crit} is also included; (b) fruit slice volume, scaled with initial volume; (c) surface-averaged temperature at the air-fruit interface; (d) corresponding water activity at the surface. The analytically-determined mass loss and drying rate for CDRP (constant drying rate period) conditions, as well as the wet bulb temperature, are indicated with the dashed grey lines. The abbreviations are detailed in Table 2.

3.3.2 Deformation modeling

The impact of including deformation in the multiphysics modeling is shown in Figure 8 and Figure 10, both for semi-conjugate and non-conjugate modeling. Not accounting for deformation decreases the drying rate significantly for both cases, which in turn affects the temperature and so on. The reason for this slower drying is straightforward: with shrinkage, the pathway for moisture to travel to the surface becomes smaller (see also Figure 7), leading to a

faster moisture removal. As a result, the impact on surface-averaged temperature and water activity is also pronounced.

3.4 Impact of peel

The impact of the peel on the drying process is shown in Figure 8, 10 and 11. Note that the peel is actually a barrier for moisture transport, but not for heat transport. As a result of the reduced surface area for evaporation (24% lower), the drying rate is lower than for the base case. However, differences are quite small, which is due to the fact that the moisture below the peel can also escape partially via the side surface. For thicker fruit slices, the impact of the peel is expected to become more pronounced. Nevertheless, a higher moisture content is found below the peel, which reduces the shrinkage in this zone. This differential shrinkage is very clear in Figure 11, with a collapse of the windward and leeward edges towards the center of the fruit (circular), and this was also observed experimentally (Figure 1). In this study, the direct relation to the drying kinetics was demonstrated. Note that the higher stiffness of the peel can also contribute to some extent, which will be looked at in a future study. As a result of the higher overall temperature of the fruit with the presence of the peel, the remaining quality at t_{crit} was also lower (Figure 9).

In Figure 12, the water activity distribution at the end of the drying process (t_{crit}) is shown for the base case and the fruit with a peel. At this point in time, the average moisture content in the fruit corresponds to an equilibrium water activity of 0.6, according to the sorption isotherm. Below this value of the water activity ($a_{w,crit}$), the risk of spoilage is reduced. However, as can be seen in Figure 12, this does not imply that the water activity is everywhere sufficiently low, as zones with a high water activity are present. If the moisture does not redistribute sufficiently fast, the risk of local spoilage is increased at these locations.

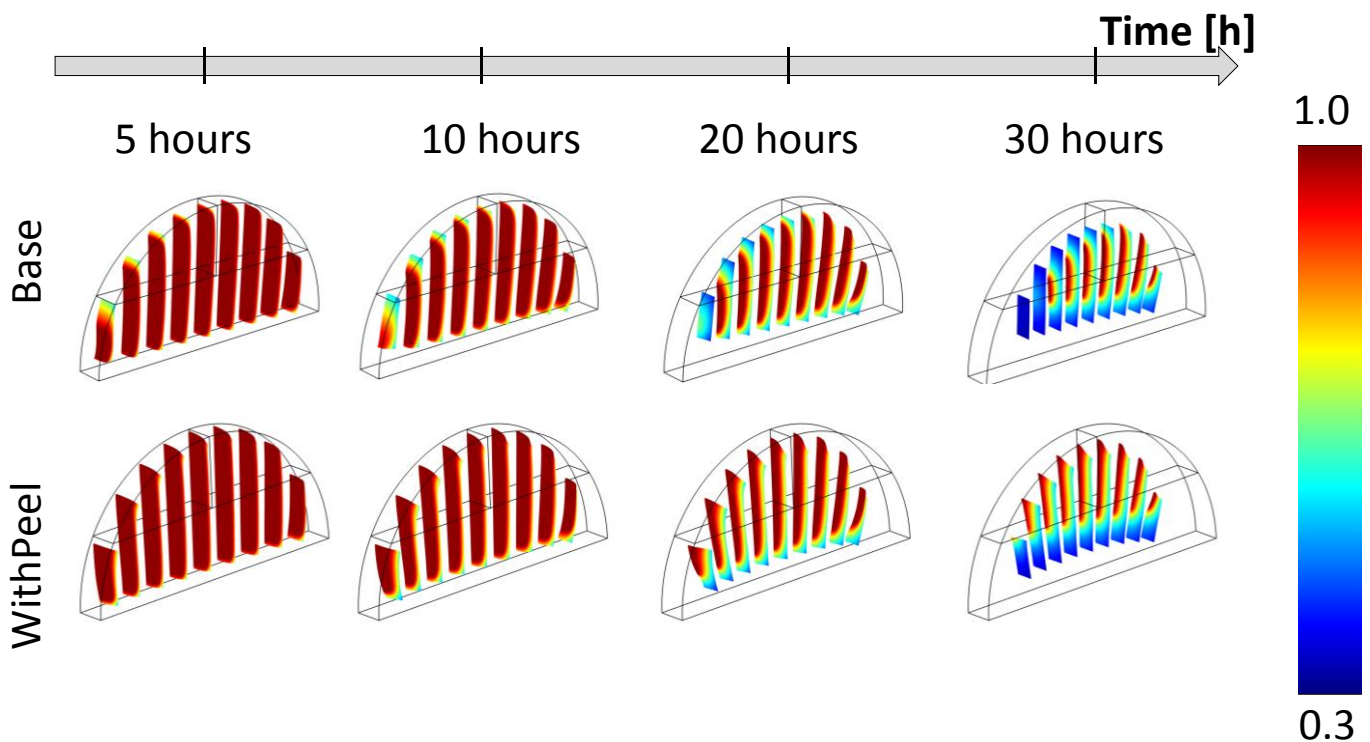


Figure 11. Water activity a_w in different vertical planes inside the fruit at different points in time for the base case and the case with a peel. The abbreviations are detailed in Table 2.

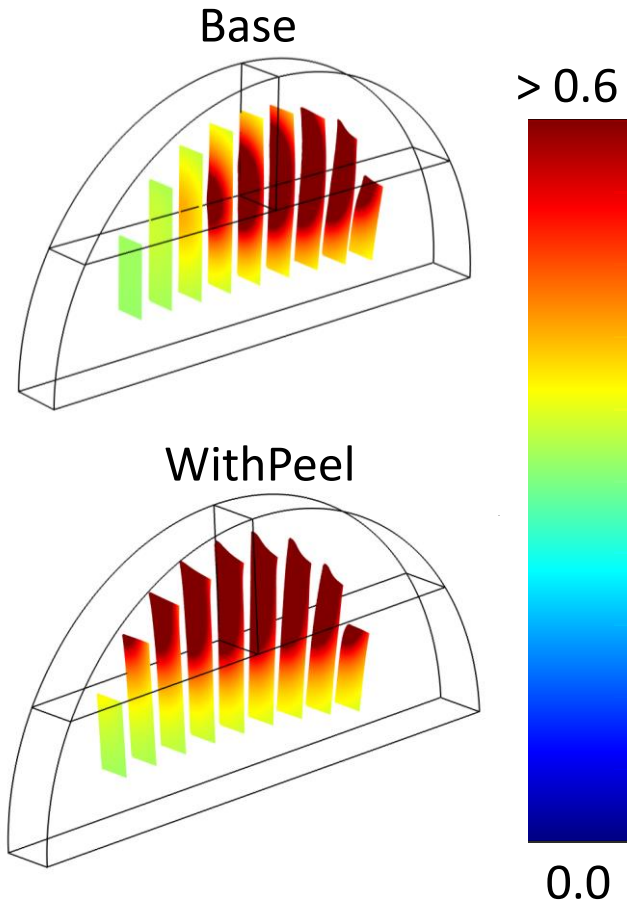


Figure 12. Water activity a_w in different vertical planes inside the fruit at the point in time (t_{crit}) during which the critical dry-matter moisture content is reached, for the base case and the case with a peel. Note that the reported water activity range goes from 0-0.6, where values > 0.6 are also represented by the same color as at 0.6.

4. Conclusions and outlook

The aim of this study was to gain more insight in the fruit drying kinetics, to investigate the impact of several modeling assumptions and to analyze the effect of the peel on the drying behavior. We identified significant differences in internal moisture distribution and deformation within the fruit slice, caused by the complex flow field around the slice. This induced large differences in convective heat/mass transfer coefficients (CTCs) between the windward, leeward and side surfaces. The need for including spatially-resolved CTCs (semi-conjugate approach) was confirmed by the large differences in drying kinetics found compared to imposing a single, constant CTC across the fruit surface (non-conjugate approach). Including deformation in the modeling also had an impact on the drying kinetics, and enhanced the drying rate. Including airflow modeling and deformation increases the computational cost and challenges solution convergence, but has a significant effect on fruit temperature. As such, modeling these

processes also influences fruit quality decay. The presence of a peel affected the drying process and the deformation, where an asymmetrical collapse towards the center of the fruit slice was observed. Coupling modeling of the hygrothermal history of the fruit during drying to fruit quality modeling opens new opportunities for optimizing drying processes. The process can be optimized not only in terms of drying time or energy consumption, but also to achieve the best product quality. We can also identify critical locations inside the fruit that can pose food safety problems. Future work should focus on evaluating different drying conditions (air speed, temperature, RH) and slice sizes in order to find the best process combination.

Acknowledgements

We acknowledge the support of the World Food System Center (WFSC) of ETH Zürich (<http://www.worldfoodsystem.ethz.ch>) and the support of the Swiss National Science Foundation SNSF (project 200021_160047). We also acknowledge Dr. Tushar Gulati, who gave invaluable advice on the mechanical modeling.

References

- [1] A.S. Mujumdar, Handbook of Industrial Drying, Fourth, CRC Press, Taylor & Francis Group, Boca Raton, USA, 2014. doi:10.1080/07373938808916399.
- [2] S. Vijayavenkataraman, S. Iniyan, R. Goic, A review of solar drying technologies, *Renew. Sustain. Energy Rev.* 16 (2012) 2652–2670. doi:10.1016/j.rser.2012.01.007.
- [3] C. Bonazzi, E. Dumoulin, Quality changes in food materials as influenced by drying processes, in: E. Tsotsas, A.S. Mujumdar (Eds.), *Mod. Dry. Technol. - Prod. Qual. Formul.*, Wiley-VHC Verlag GmbH, Weinheim, Germany, 2011: pp. 1–20.
- [4] T. Defraeye, Advanced computational modelling for drying processes - A review, *Appl. Energy*. 131 (2014) 323–344. doi:10.1016/j.apenergy.2014.06.027.
- [5] P.H.S. Santos, M. a. Silva, Retention of Vitamin C in Drying Processes of Fruits and Vegetables — A Review, *Dry. Technol.* 26 (2008) 1421–1437. doi:10.1080/07373930802458911.
- [6] T. Defraeye, P. Verboven, Moisture barriers to control drying of fresh-cut fruit: Quantifying their impact by modeling, *Food Bioprod. Process.* 101 (2017) 205–213. doi:10.1016/j.fbp.2016.10.016.
- [7] M. Vargas, C. Pastor, A. Chiralt, D.J. McClements, C. Gonzalez-Martinez, Recent advances in edible coatings for fresh and minimally processed fruits, *Crit. Rev. Food Sci. Nutr.* 48 (2008) 496–511. doi:10.1080/10408390701537344.

- [8] R.K. Dhall, Advances in edible coatings for fresh fruits and vegetables: a review., *Crit. Rev. Food Sci. Nutr.* 53 (2013) 435–50. doi:10.1080/10408398.2010.541568.
- [9] P. Laurienzo, M. Di Stasio, M. Malinconico, M.G. Volpe, De-hydration of apples by innovative bio-films drying, *J. Food Eng.* 97 (2010) 491–496. doi:10.1016/j.jfoodeng.2009.11.006.
- [10] T. Defraeye, B. Nicolai, D. Mannes, W. Aregawi, P. Verboven, D. Derome, Probing inside fruit slices during convective drying by quantitative neutron imaging, *J. Food Eng.* 178 (2016) 198–202. doi:10.1016/j.jfoodeng.2016.01.023.
- [11] B.M. Nicolai, T. Defraeye, B. De Ketelaere, E. Herremans, M.L. a T.M. Hertog, W. Saeys, A. Torricelli, T. Vandendriessche, P. Verboven, Nondestructive measurement of fruit and vegetable quality., *Annu. Rev. Food Sci. Technol.* 5 (2014) 285–312. doi:10.1146/annurev-food-030713-092410.
- [12] E. Herremans, A. Melado-Herreros, T. Defraeye, B. Verlinden, M. Hertog, P. Verboven, J. Val, M.E. Fernández-Valle, E. Bongaers, P. Estrade, M. Wevers, P. Barreiro, B.M. Nicolai, Comparison of X-ray CT and MRI of watercore disorder of different apple cultivars, *Postharvest Biol. Technol.* 87 (2014) 42–50. doi:10.1016/j.postharvbio.2013.08.008.
- [13] T. Defraeye, V. Lehmann, D. Gross, C. Holat, E. Herremans, P. Verboven, B.E. Verlinden, B.M. Nicolai, Application of MRI for tissue characterisation of “Braeburn” apple, *Postharvest Biol. Technol.* 75 (2013) 96–105. doi:10.1016/j.postharvbio.2012.08.009.
- [14] A. Warning, P. Verboven, B. Nicola??, G. Van Dalen, A.K. Datta, Computation of mass transport properties of apple and rice from X-ray microtomography images, *Innov. Food Sci. Emerg. Technol.* 24 (2014) 14–27. doi:10.1016/j.ifset.2013.12.017.
- [15] A. Dhall, A.K. Datta, Transport in deformable food materials: A poromechanics approach, *Chem. Eng. Sci.* 66 (2011) 6482–6497. doi:10.1016/j.ces.2011.09.001.
- [16] T. Gulati, A.K. Datta, Mechanistic understanding of case-hardening and texture development during drying of food materials, *J. Food Eng.* 166 (2015) 119–138. doi:10.1016/j.jfoodeng.2015.05.031.
- [17] T. Defraeye, P. Verboven, Convective drying of fruit: Role and impact of moisture transport properties in modelling, *J. Food Eng.* 193 (2017) 95–107. doi:10.1016/j.jfoodeng.2016.08.013.
- [18] P. Caccavale, M.V. De Bonis, G. Ruocco, Conjugate heat and mass transfer in drying: A modeling review, *J. Food Eng.* 176 (2016) 28–35. doi:10.1016/j.jfoodeng.2015.08.031.
- [19] T. Gulati, H. Zhu, A.K. Datta, Coupled electromagnetics, multiphase transport and large deformation model for microwave drying, *Chem. Eng. Sci.* 156 (2016) 206–228. doi:10.1016/j.ces.2016.09.004.
- [20] İ. Ceylan, M. Aktaş, H. Doğan, Mathematical modeling of drying characteristics of tropical fruits, *Appl. Therm. Eng.* 27 (2007) 1931–1936. doi:10.1016/j.applthermaleng.2006.12.020.

- [21] K. Chapchaimoh, N. Poomsa-Ad, L. Wiset, J. Morris, Thermal characteristics of heat pump dryer for ginger drying, *Appl. Therm. Eng.* 95 (2016) 491–498. doi:10.1016/j.applthermaleng.2015.09.025.
- [22] I. Zlatanović, M. Komatina, D. Antonijević, Low-temperature convective drying of apple cubes, *Appl. Therm. Eng.* 53 (2013) 114–123. doi:10.1016/j.applthermaleng.2013.01.012.
- [23] B. Sturm, A.M. Nunez Vega, W.C. Hofacker, Influence of process control strategies on drying kinetics, colour and shrinkage of air dried apples, *Appl. Therm. Eng.* 62 (2014) 455–460. doi:10.1016/j.applthermaleng.2013.09.056.
- [24] T. Defraeye, When to stop drying fruit: Insights from hygrothermal modelling, *Appl. Therm. Eng.* 110 (2017) 1128–1136. doi:10.1016/j.applthermaleng.2016.08.219.
- [25] W.A. Aregawi, T. Defraeye, P. Verboven, E. Herremans, G. De Roeck, B.M. Nicolai, Modeling of Coupled Water Transport and Large Deformation During Dehydration of Apple Tissue, *Food Bioprocess Technol.* 6 (2013) 1963–1978. doi:10.1007/s11947-012-0862-1.
- [26] N.D. Mrad, C. Bonazzi, N. Boudhrioua, N. Kechaou, F. Courtois, Moisture Sorption Isotherms, Thermodynamic Properties, and Glass Transition of Pears and Apples, *Dry. Technol.* 30 (2012) 1397–1406. doi:10.1080/07373937.2012.683843.
- [27] T. Lu, H.L. Wang, P.X. Jiang, A Thermo-Hydro-Mechanics Bidirectional Coupling Mathematical Model for Drying of Biological Porous Medium, *Dry. Technol.* 33 (2015) 420–428. doi:10.1080/07373937.2014.970260.
- [28] W. Aregawi, T. Defraeye, S. Saneinejad, P. Vontobel, E. Lehmann, J. Carmeliet, D. Derome, P. Verboven, B. Nicolai, Dehydration of apple tissue: Intercomparison of neutron tomography with numerical modelling, *Int. J. Heat Mass Transf.* 67 (2013) 173–182. doi:10.1016/j.ijheatmasstransfer.2013.08.017.
- [29] ASHRAE, *ASHRAE Handbook - Refrigeration: systems and applications (SI edition)*, Atlanta, 2010. <http://catalog.hathitrust.org/Record/000065913%5Cnhttp://hdl.handle.net/2027/mdp.39015010995705> (1986)%5Cn<http://hdl.handle.net/2027/mdp.39015011136614> (1986)%5Cn<http://hdl.handle.net/2027/mdp.39015023284907> (1990).
- [30] G.L. Robertson, *Food Packaging: Principles and Practice*, Third Edition, Third, Taylor & Francis Group LLC, Boca-Raton, 2016. doi:10.1177/0340035206070163.
- [31] M.A.J.S. Van Boekel, Kinetic Modeling of Food Quality: A Critical Review, *Compr. Rev. Food Sci. Food Saf.* 7 (2008) 144–158. doi:10.1111/j.1541-4337.2007.00036.x.
- [32] T. Defraeye, Towards more efficient intermittent drying of fruit: Insights from combined hygrothermal-quality modelling, *Innov. Food Sci. Emerg. Technol.* 38 (2016) 262–271. doi:10.1016/j.ifset.2016.10.003.
- [33] J.F. Thompson, Pre-cooling and storage facilities, in: USDA (Ed.), *USDA Agric. Handb. Number 66 Commer. Storage Fruits, Veg. Flor. Nurs. Stock.*, USDA, 2004: pp. 1–10. <http://www.ba.ars.usda.gov/hb66/contents.html>.

- [34] F.R. Menter, Two-Equation Eddy-Eiscosity Turbulence Models for Engineering Applications, *AIAA J.* 32 (1994) 1598–1605. doi:10.2514/3.12149.
- [35] M. Casey, T. Wintergerste, Special Interst Group on “Quality and Trust in Industrial CFD” Best Practice Guidelines, First edit, ERCOFTAC, 2000.
- [36] T. Defraeye, P. Verboven, B. Nicolai, CFD modelling of flow and scalar exchange of spherical food products: Turbulence and boundary-layer modelling, *J. Food Eng.* 114 (2013) 495–504. doi:10.1016/j.jfoodeng.2012.09.003.
- [37] T. Defraeye, E. Herremans, P. Verboven, J. Carmeliet, B. Nicolai, Convective heat and mass exchange at surfaces of horticultural products: A microscale CFD modelling approach, *Agric. For. Meteorol.* 162–163 (2012) 71–84. doi:10.1016/j.agrformet.2012.04.010.
- [38] A. Kaya, O. Aydin, I. Dincer, Numerical modeling of heat and mass transfer during forced convection drying of rectangular moist objects, *Int. J. Heat Mass Transf.* 49 (2006) 3094–3103. doi:10.1016/j.ijheatmasstransfer.2006.01.043.
- [39] M. Ateeque, Udayraj, R.K. Mishra, V.P. Chandramohan, P. Talukdar, Numerical modeling of convective drying of food with spatially dependent transfer coefficient in a turbulent flow field, *Int. J. Therm. Sci.* 78 (2014) 145–157. doi:10.1016/j.ijthermalsci.2013.12.003.
- [40] T. Defraeye, A. Radu, Convective drying of fruit: a deeper look at the air-material interface by conjugate modelling, *Int. J. Heat Mass Transf.* 108 (2017) 1610–1622. doi:10.1016/j.ijheatmasstransfer.2017.01.002.
- [41] T. Defraeye, B. Blocken, J. Carmeliet, Analysis of convective heat and mass transfer coefficients for convective drying of a porous flat plate by conjugate modelling, *Int. J. Heat Mass Transf.* 55 (2012) 112–124. doi:10.1016/j.ijheatmasstransfer.2011.08.047.
- [42] S. Ben Mabrouk, E. Benali, H. Oueslati, Experimental study and numerical modelling of drying characteristics of apple slices, *Food Bioprod. Process.* 90 (2012) 719–728. doi:10.1016/j.fbp.2012.02.001.
- [43] W. a. M. McMinn, T.R. a. Magee, Principles, Methods and Applications of the Convective Drying of Foodstuffs, *Food Bioprod. Process.* 77 (1999) 175–193. doi:10.1205/096030899532466.